Dalton Transactions

Accepted Manuscript

ROYAL SOCIETY OF CHEMISTRY

www.rsc.org/dalton

Dalton Transactions

Dynamic Article Links ►

Cite this: DOI: 10.1039/c0xx00000x

www.rsc.org/dalton

ARTICLE TYPE

Growth mechanism and photocatalytic activity of self-organized N-doped $(BiO)_2CO_3$ hierarchical nanosheets microspheres from bismuth citrate and urea

Fan Dong[a*], Ting Xiong[a], Rui Wang[a], Yanjuan Sun[a*], Yanke Jiang[a]

Received (in XXX, XXX) Xth XXXXXXXXX 20XX, Accepted Xth XXXXXXXXX 20XX
DOI: 10.1039/b000000x

Abstract: Synthesis of nano-/microstructured functional materials with 3D hierarchical microspheres structure has provided new opportunities for optimizing their physical and chemical properties. This work revealed a new growth mechanism of self-organized N-doped $(BiO)_2CO_3$ hierarchical microspheres which were fabricated by hydrothermal treatment of bismuth citrate and urea without additive. Based on time-dependent observation, several evolution processes were believed to account for the formation of the self-organized N-doped $(BiO)_2CO_3$ hierarchical microspheres. Initially, crystallized $(BiO)_4CO_3(OH)_2$ particles were formed during the nucleation and crystallization process. Subsequently, the intermediate $(BiO)_4CO_3(OH)_2$ reacted with CO_3^{2-} to generate $(BiO)_2CO_3$ growth nuclei on the surface of the CO_2 bubbles which can act as heterogeneous nucleation centers. Next, the $(BiO)_2CO_3$ growth nuclei aggregated together after the consumption of CO_2 bubbles with the increased concentration of OH^- and further grew to be nanosheets. The microspheres constructed by small nanosheets were further grown at the consumption of small particles. Finally, all $(BiO)_4CO_3(OH)_2$ transformed to $(BiO)_2CO_3$ phase, accompanied with the doping of N element into the lattice of $(BiO)_2CO_3$, and thereby, the well-defined N-doped $(BiO)_2CO_3$ hierarchical microspheres were shaped. Depending on the distance between neighboring CO_2 bubbles, the resultant microspheres can be linked or dispersed. Besides, the gradual release of CO_2 bubbles and CO_3^{2-} played a crucial role in controlling the nucleation and growth process, resulting in different size of microspheres. The fabricated N-doped $(BiO)_2CO_3$ hierarchical microspheres displayed admirable efficient and duralbe photocatalytic activity under both UV and visible light towards removal of NO, which is mainly attributed to the introduction of N element and the special hierarchical structure. This work provides new insights into the controlled synthesis of photocatalytic nano/microstructures for potential environmental and energetic applications.

1. Introduction

Recently, research on three dimensional (3D) hierarchical microspheres structure has been a thriving and exciting field for their potential applications in photocatalysts, drugs delivery, photovoltaics, sensors and supercapacitors.[1-5] Among which, 3D photocatalysts, displaying admirable photoactivity because of the unique properties, such as large surface areas, special pore structure, efficient light harvesting and charge separation, subsequently allowing their application in energy conversion and environment treatment, have been under extensive study and fabrication.[6-7]

To date, template and template-free syntheses are the two most widely used methods to prepare photocatalytic

[a] Chongqing Key Laboratory of Catalysis and Functional Organic Molecules, College of Environmental and Biological Engineering, Chongqing Technology and Business University, Chongqing, 400067, China
* To whom correspondence should be addressed.
E-mail: dfctbu@126.com (Fan Dong), syhsyj@163.com (Yanjuan Sun).
Tel.: +86-23-62769785-605; Fax: +86-23-62769785-605.

materials with 3D hierarchical microspheres structures. The template assisted approaches, including soft templates and hard templates which are generally utilized to control the process of nucleation, growth and arrangement, have been considered to be quite effective for the fabrication of 3D microspheres. [8-11] However, these approaches typically tend to be rather complicated, and the final products may suffer from the residual of heterogeneous impurities or the damage of the structural integrity. Of particular note is the soft template included in the template syntheses, which is a truly simple and economical method if involving gaseous template. Zhang and co-workers recently prepared $Sn_2Nb_2O_7$ microsphere via the CO_2 and NH_3 bubbles generated from urea as soft templates.[12] Likewise, $K_4Nb_6O_{17}$[13] and $BiVO_4$[14] microspheres were fabricated by other research groups though the similar methods which are based on bubbles acting as soft templates.

Template-free synthetic methods as environmentally benign and economical methods have received increasing attention. Various known physical phenomena, such as Ostwald Ripening, Rriented Attachment and Kirkendall effect, have been adopted to direct the low-dimensional building blocks to build the 3D structures.[15-18] For instance, Cui's group prepared $FeMoO_4$ hollow nanospheres by a chemical conversion-induced method accompanied with Ostwald ripening process.[19] Liu et al. synthesized hierarchical BiOI nests via the Kirkendall effect.[20] Jiang and co-workers fabricated Fe-doped BiOBr hollow microspheres though both oriented attachment and Ostwald ripening.[21]

Very recently, much attention has been focused on $(BiO)_2CO_3$ largely owing to its promising antibacterial performance and photocatalytic activity. Usually, controlling the shape of photocatalysts allows us to control the properties of the materials, so various morphologies of $(BiO)_2CO_3$ especially 3D hierarchical structures have been fabricated to exploit its outstanding properties. For example, Xie's group have synthesized $(BiO)_2CO_3$ flowers by a hydrothermal process using $Bi(NO_3)_3$ and citric acid as precursors involved Ostwald ripening. [22] Yin et al. have prepared flower-like $(BiO)_2CO_3$ by a precipitation method using CTAB as template (soft template method).[23] $(BiO)_2CO_3$ hierarchical hollow microspheres were fabricated by our group through a template-free method based on a unique process of dissolution, crystallization and Ostwald ripening.[24-25] Unfortunately, the pure $(BiO)_2CO_3$ semiconductor has a quite wide band gap (3.1-3.5 eV), which limits its exploitation of solar energy. Nitrogen doping has been extensively employed to narrow the band gap.[26-27] In our previous work, we have developed a one-pot additive-free method to fabricate *in situ* N-doped $(BiO)_2CO_3$ microspheres by hydrothermal treatment of bismuth citrate and urea, and the as-prepared samples showed fascinating photocatalytic activity.[28] Yet, the growth mechanism of this special architecture is unclear. To our knowledge, it remains an ongoing challenge to develop simple and reliable synthetic methods for hierarchically self-assembled architectures. Thus, exploring the growth mechanism of self-organized N-doped $(BiO)_2CO_3$ hierarchical nanosheets microspheres with additive-free method is highly desired and necessary.

Herein, a formation process of N-doped $(BiO)_2CO_3$ hierarchical microspheres from bulk to microspheres was observed. To give a better understanding of the formation mechanism of self-organized N-doped $(BiO)_2CO_3$ hierarchical microspheres structure, we fabricated products of different stages in a hydrothermal treatment involving bismuth citrate and urea as the starting materials through time control. These products were systematically investigated in the aspects of the crystal structure, chemical composition and morphology by XRD, FT-IR, SEM, TEM, XPS, UV-vis DRS and BET-BJH in detail. Upon observing the morphology transformation, a new growth mechanism of novel N-doped $(BiO)_2CO_3$ hierarchical microspheres assembled from interconnected nanosheets was proposed. The as-prepared N-doped $(BiO)_2CO_3$ hierarchical microspheres exhibited efficient and durable photocatalytic activity for removal of NO in air under both visible and UV light irradiation. This work demonstrated here is expected to provide new insights into the controllable synthesis of other 3D hierarchical microspheres structures.

2. Experimental Section

2.1 Synthesis

All chemicals were of analytic grade (Sigma Aldrich) and used without further purification in this study. Distilled water was used throughout this experiment. In a typical synthesis, 1.60 g of bismuth citrate and 0.72 g of urea (the molar ratio of bismuth citrate and urea is 1:3) were dissolved in 75 mL of H_2O and stirred for 30 min. The resulted aqueous solution was transferred into a 100 mL of autoclave Teflon vessel, which was then hydrothermally treated at 180 ^oC for a series of reaction times. To observe the growth process and substantially understand the growth mechanism of self-organized N-doped $(BiO)_2CO_3$ hierarchical microspheres, the hydrothermal time was varied from 0 to 48h (e.g., 0, 3, 6, 9, 12, 24, 48 h). The resultant precipitates obtained at different time were collected by centrifugation, rinsed with water and ethanol three times, and dried at 60 ^oC to get final samples without further treatment, respectively. For comparison, the commercial Degussa P25 was used as a reference sample.

2.2 Characterization

The crystal phase was analyzed by X-ray diffraction with Cu Kα radiation (XRD: model D/max RA, Japan). A scanning electron microscope (SEM, JEOL model JSM-6490, Japan) was used to characterize the morphology of

the samples. The morphology and structure were examined by transmission electron microscopy (TEM: JEM-2010, Japan). X-ray photoelectron spectroscopy with Al KαX-rays (hν=1486.6 eV) radiation (XPS: Thermo ESCALAB 250, USA) was used to investigate the surface properties and to probe the total density of the state (DOS) distribution in the valence band. The shift of the binding energy was corrected using the C1s level at 284.8 eV as an internal standard. Nitrogen adsorption-desorption isotherms were obtained on a nitrogen adsorption apparatus (ASAP 2020, USA) with all samples degassed at 150 ^{o}C prior to measurements. FT-IR spectra were recorded on a Nicolet Nexus spectrometer on samples embedded in KBr pellets. The UV-vis diffuse reflection spectra were obtained for the dry-pressed disk samples using a Scan UV-vis spectrophotometer (UV-vis DRS: UV-2450, Shimadzu, Japan) equipped with an integrating sphere assembly, using $BaSO_4$ as reflectance sample.

2.3 Evaluation of photocatalytic activity

The photocatalytic activities of the as-prepared samples obtained from different time were evaluated by removal of NO at ppb level in a continuous flow reactor at ambient temperature. The volume of the rectangular reactor, made of stainless steel and covered with Saint-Glass, was 4.5 L (30 cm × 15 cm × 10 cm). For the visible light photocatalytic activity test, a 300 W commercial tungsten halogen lamp (General Electric) was used as the irradiation source, and a UV cutoff filter (420 nm) was applied to remove UV light in the light beam. The lamp was vertically placed outside the reactor in an appropriate distance, and four mini-fans were used to cool the lamp and flow system. For the UV light photocatalytic activity test, two 6W UV lamps (Cole-Parmler), emitting a primary wavelength at 365 nm was used. The as-prepared photocatalysts of 0.15g was added into 30 mL of H_2O and sonicated for 10 min. The resultant suspension was coated onto a dish with a diameter of 12.0 cm, and then pretreated at 70 ^{o}C to remove water. For each photocatalytic activity test, two sample dishes containing photocatalyst powder will be used. The NO gas was acquired from a compressed gas cylinder at a concentration of 100 ppm of NO (N2 balance, BOC gas) with traceable National Institute of Standards and Technology (NIST) standard. The initial concentration of NO was diluted to about 450 ppb by the air stream supplied by a zero air generator (Thermo Environmental Inc., model 111). The desired relative humidity (RH) level of the NO flow was controlled at 70% by passing the zero air streams through a humidification chamber. The gas streams were premixed completely by a gas blender, and the flow rate was controlled at 3.3 L/min by a mass flow controller. After the adsorption-desorption equilibrium was achieved, the lamp was turned on. The concentration of NO was continuously measured by a chemiluminescence NO analyzer (Thermo Environmental Instruments Inc., model 42c), which monitors NO, NO_2, and NOx (NOx represents NO +NO_2) with a sampling rate of 0.7 L/min. The removal efficiency (η) of NO was calculated as $\eta\ (\%) = (1 - C/C_0) \times 100\%$, where C_0 and C are concentrations of NO in the feeding steam and the outlet stream, respectively. The kinetics of photocatalytic NO removal reaction is a pseudo first-order reaction at low NO concentration as $\ln(C_0/C)=kt$, where k is the Arrhenius rate constant.

3. Results and discussion

3.1 Phase structure. The crystal structures of the as-prepared samples obtained at different reaction time were characterized by X-ray diffraction (XRD, Fig. 1a). The diffraction peaks of the as-prepared sample obtained at 3h can be indexed to $Bi(C_6H_5O_7)$ phase, which tells us that $Bi(C_6H_5O_7)$ hardly participates in reaction before 3h. As we know, urea can be decomposed to produce NH_3 and CO_2 gradually (reactions (1)) when the temperature exceeds 80^{o}C, then reaction (2) and (3) will take place. When the reaction time is prolonged to 6h, the diffraction peaks of bismuth citrate are disappeared, implying that bismuth citrate is hydrolyzed. Bismuth citrate can be hydrolyzed by OH^- arising from reaction (2), generating different types of ions (reactions (4)).[29] After that, some ions (reactions (5)) react with each other to generate $(BiO)_4CO_3(OH)_2$ during this stage.

$$NH_2CONH_2 + H_2O \rightarrow 2NH_3 + CO_2 \quad (1)$$

$$NH_3 + H_2O \rightarrow NH_4^+ + OH^- \quad (2)$$

$$CO_2 + 2\ OH^- \rightarrow CO_3^{2-} + H_2O \quad (3)$$

$$Bi(C_6H_5O_7) + 3OH^- \rightarrow BiO^+ + C_6H_5O_7^{3-} + 3H^+ \quad (4)$$

$$4BiO^+ + CO_3^{2-} + 2OH^- \rightarrow (BiO)_4CO_3(OH)_2\ (s) \quad (5)$$

Apparently, the XRD pattern could be assigned to $(BiO)_4CO_3(OH)_2$ (JCPDS-ICDD Card No. 38-0579), indicating that $(BiO)_4CO_3(OH)_2$ is formed at an early reaction stage. Although the diffraction patterns of $(BiO)_4CO_3(OH)_2$ and $(BiO)_2CO_3$ are similar, the peaks of $(BiO)_4CO_3(OH)_2$ occur at lower angles and some peaks are not pronounced.[30] Here the weak and wide diffraction peaks of the sample also show the poor crystallinity. Notably, the as-obtained $(BiO)_4CO_3(OH)_2$ can react with CO_3^{2-} to form $(BiO)_2CO_3$ (reaction (6)), and the OH^- stemming from reaction (6) may take part in reaction (3), (4) or (5). However, only a small fraction of CO_3^{2-} are likely to participate in reaction (6) because this stage is governed by reaction (5), consequently yielding a relatively low concentration of $(BiO)_2CO_3$. The diffraction peaks of $(BiO)_2CO_3$ are not observed because they are much weak and can be overlapped by the peaks of $(BiO)_4CO_3(OH)_2$. Reaction (5) continues to proceed but slowly with the increasing time. As a result, the XRD pattern of the sample derived from 9h is similar to the sample from 6h. By extending the reaction time from 9h to12h, peaks are more pronounced. Moreover, further observation signifies

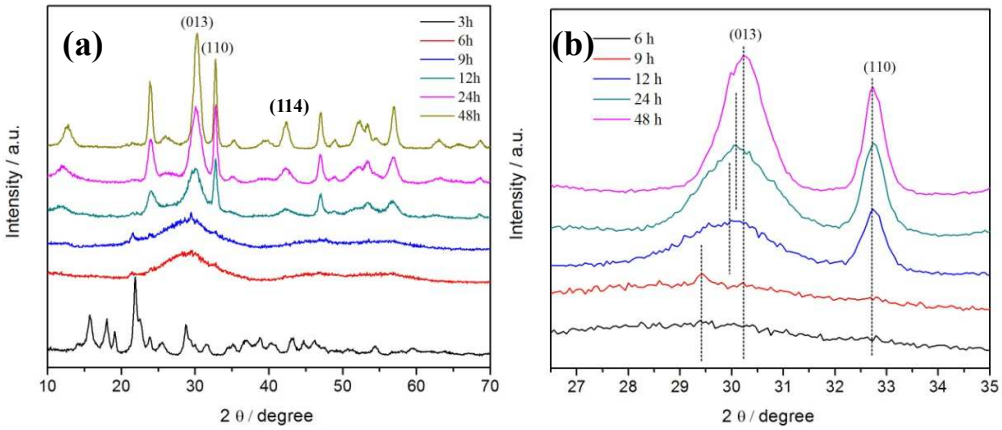

Fig. 1 XRD patterns (a) for samples obtained at different reaction time from 3 to 48 h, and (b) enlarged view of (013) and (110) diffraction region.

that the diffraction angles shift to higher values (Fig. 1b). These phenomena can be explained by the transformation of most $(BiO)_4CO_3(OH)_2$ phase to $(BiO)_2CO_3$, and thereby, the obtained sample is a mixed phase containing $(BiO)_4CO_3(OH)_2$ and $(BiO)_2CO_3$. With the consumption of CO_3^{2-} and the production of OH^-, the citrate ions start to decompose to yield CO_2 (reaction (7)). Some CO_2 are soluble in alkali to generate CO_3^{2-} (reaction (3)), then CO_3^{2-} will take part in reaction (6). Considering the production of amount of $(BiO)_2CO_3$, we can speculate that reaction (7) predominantly happens in this stage.

$$(BiO)_4CO_3(OH)_2(s) + CO_3^{2-} \rightarrow 2(BiO)_2CO_3(s) + 2\ OH^- \quad (6)$$

$$C_6H_5O_7^{3-} \rightarrow CO_2 + H_2O \quad (7)$$

As the reaction proceeds, CO_3^{2-} continues to react with $(BiO)_4CO_3(OH)_2$ to produce $(BiO)_2CO_3$, so the diffraction angles shift to higher values and the relative intensity of the diffraction peaks becomes stronger when reaction time extends 24h. For the samples achieved at 48h, the diffraction peaks become much stronger and can be indexed to $(BiO)_2CO_3$ phase (JCPDS-ICDD Card No.41-1488). Furthermore, the diffraction angle of the (013) peak shifting to 30.3° also demonstrates that all the $(BiO)_4CO_3(OH)_2$ samples are converted to $(BiO)_2CO_3$ phase after 48h of reaction. Additionally, the (013) and (110) diffraction peaks of the samples increase in intensity and decrease in width at half-height due to the enhancement of crystallinity with increasing time as observed in the enlarged view (Fig. 1b). The enhanced (110) diffraction peak suggests that as-prepared samples have a preferential growth along the (110) plane. Quite significantly, N element can be doped into the lattice of $(BiO)_2CO_3$ during the formation process, ultimately modifying the band structure.

According to the crystal structure of $(BiO)_2CO_3$, the $(BiO)_2^{2+}$ layers and CO_3^{2-} layers are inter-grown with the plane of the CO_3^{2-} group orthogonal to the plane of the $(BiO)_2^{2+}$ layer.[31] The Bi^{3+} with [8]-coordination shows stereo active lone-pair behavior that may contribute to the Bi–O polyhedron with large distortion. Such an internal layered structure would guide the lower growth rate along a certain axis to form 2D nanosheet morphology.[32]

3.2 FT-IR spectra. FT-IR spectra were adopted to directly observe the chemical composition of the samples from 0h to 48h. As illustrated in Fig. 2, the absorption bands of the samples obtained at 0h and 3h are similar, and they are distinctly different from other samples due to the samples are composed of $Bi(C_6H_5O_7)$, which are consistent with XRD result. When reaction time achieves 6h, the peaks of CO_3^{2-} and OH^- can be observed. The ''free'' CO_3^{2-} (point group symmetry D3h) has four internal vibrations, including symmetric stretching mode ν_1 (1068 cm^{-1}), the anti-symmetric vibration ν_3 (1465 and 1390 cm^{-1}), the out-of-plane bending mode ν_2 (845 and 821 cm^{-1}), and the in-plane deformation ν_4 (698 and 670 cm^{-1}), $\nu_1 + \nu_4$ (1756 and 1730 cm^{-1}).[33] Moreover, the peak intensity associated with CO_3^{2-} increases with prolonged reaction time.

The broad peaks in the range of 1500–1600 and 3300–3600 cm^{-1} regions in Fig. 2a and 2b correspond to the stretching vibrations and deformation vibrations of OH^- including hydroxyl groups and molecular water.[28,34] It is noteworthy that the peak intensity of hydroxyl groups decreases gradually with prolonged reaction time. Particularly, the intensity of the peak at 1520 cm^{-1} obviously decreases mainly due to the substitution of OH^- by CO_3^{2-} in $(BiO)_4CO_3(OH)_2$. Since the final $(BiO)_2CO_3$ sample derived from 48 h contains no OH^- groups, the OH^- groups detected by FT-IR may come from the H_2O molecule absorbed on the surface. The surface hydroxyl groups are expected to play an important role in photocatalysis.

Generally speaking, OH^- groups exist in $(BiO)_4CO_3(OH)_2$ while are absent in $(BiO)_2CO_3$. The decrease of OH^- groups and enhancement of CO_3^{2-} in peak intensity provide strong evidence for the gradual transformation of $(BiO)_4CO_3(OH)_2$ to $(BiO)_2CO_3$ during a prolonged hydrothermal reaction. Careful observation in the FT-IR spectra

implies that the peak position also varies with increasing reaction time, which can be attributed to the variation of chemical environment of the bonds during structural evolution. XRD combined with FTIR reveal that an intermediate $(BiO)_4CO_3(OH)_2$ is initially produced and then the CO_3^{2-} substituting for OH^- in $(BiO)_4CO_3(OH)_2$ would result in the formation of $(BiO)_2CO_3$ phase.

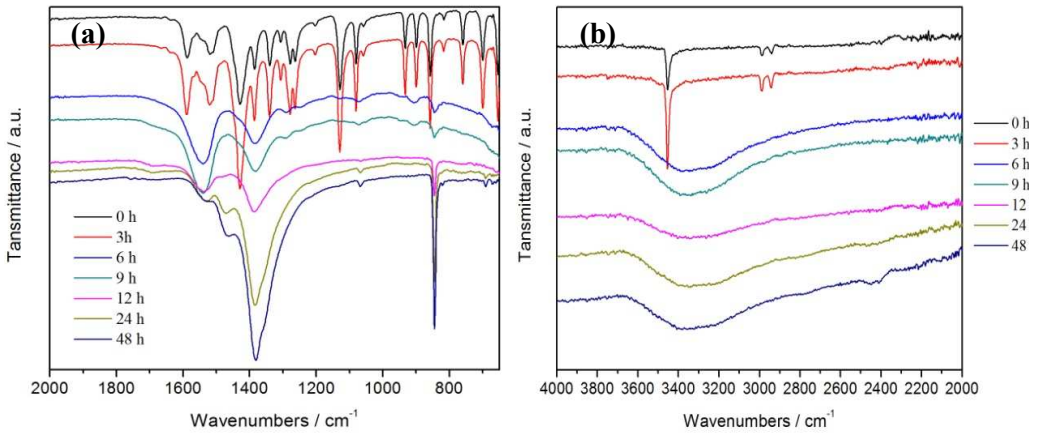

Fig. 2 FT-IR spectra of the samples treated for different reaction time from 0 to 48 h in the range of 650–2000 cm^{-1}(a) and 2000–4000 cm^{-1}(b).

3.3 Morphological evolution. To obtain a better understanding of the formation mechanism of the self-organized N-doped $(BiO)_2CO_3$ microspheres, products generated from different growth stages were collected for SEM measurements as shown in Fig. 3. We can observe that the precursors are irregular particles with rough surfaces before the reaction (Fig. 3a). When the reaction is carried out for 3h, the morphology of obtained samples (Fig. 3b) is similar to that of the samples collected at 0 h, and the bulk coexisting with some particles is bismuth citrate before 3h as revealed by XRD.

When the reaction lasts for 6h, as illustrated in Fig. 3c and 3d, large amounts of regular particles with uniform size are produced. Based on the XRD analysis, Bismuth citrate is first hydrolyzed and decomposed to generate different types of ions during this stage. Then some ions react with each other (reaction (5)) to form the $(BiO)_4CO_3(OH)_2$ growth nuclei. The amorphous nuclei grow to crystallize and small particles are generated. Therefore, the component of these particles is $(BiO)_4CO_3(OH)_2$. Besides, we can find a few small microspheres with particles around. In this stage, certain free CO_2 bubbles mainly originating from urea can exist in the solution for a certain time, which can act as heterogeneous nucleation centers according to the literatures.[35-37] $(BiO)_4CO_3(OH)_2$ can react with CO_3^{2-} to produce $(BiO)_2CO_3$. Thus, it is supposed that the $(BiO)_2CO_3$ growth nuclei are initially generated on the surface of CO_2 bubbles. With the increasing concentration of OH^- (reaction (6)), CO_2 bubbles will disappear, then these $(BiO)_2CO_3$ growth nuclei on the surface of CO_2 bubbles tend to aggregate together by the driving force, which can serve as growth centers. Since the internal layered structure of $(BiO)_2CO_3$ would guide the lower growth rate along a certain axis to form 2D nanosheet morphology,[32] the $(BiO)_2CO_3$ growth nuclei further grow to be nanosheets with the transformation from $(BiO)_4CO_3(OH)_2$ to $(BiO)_2CO_3$ by means of dissolution-reaction-crystallization process. Meantime, N element can be doped into the lattice of $(BiO)_2CO_3$ during the transformation process. Naturally, N-doped $(BiO)_2CO_3$ microspheres constructed by nanosheets are formed, and these nanosheets are packed from center to edge layer by layer to form hierarchical nanostructure. However, only a few microspheres can be achieved possibly because of the small amount of CO_2 bubbles.

Upon further increasing the time to 9 h, it is found in Fig. 3e and 3f that the size of the particles becomes smaller, which can be considered as the consequence of the dissolution and recrystallization of $(BiO)_4CO_3(OH)_2$ particles, The microspheres become bigger by the consumption of particles around. Simultaneously, some new microspheres can be observed, which may be attributed to the release of CO_2 generated by citrate ions. Citrate ions can be decomposed to produce CO_2 as shown in reaction (7), some CO_2 are soluble in alkali to give rise to carbonate ions and others keep CO_2 bubbles state. Nevertheless, only a few citrate ions are decomposed in this stage. Notably, depending on the distance between neighboring CO_2 bubbles, the resultant microspheres can be stacked together or dispersed. By prolonging the reaction time to 12h, from Fig. 3g and 3h, we can observe much more linked or dispersed microspheres which are in different size. Many particles attach on the surface of the microspheres and show preferential oriented attachment growth. Hence, citrate ions are considered to be decomposed to produce abundant CO_2 predominantly in this stage. Higher CO_2 and CO_3^{2-} concentration can result

in a higher nuclei concentration and higher growth rates of the nanosheets. Also, the inhomogeneous release of CO_2 bubbles and CO_3^{2-} are responsible for the different size of microspheres.

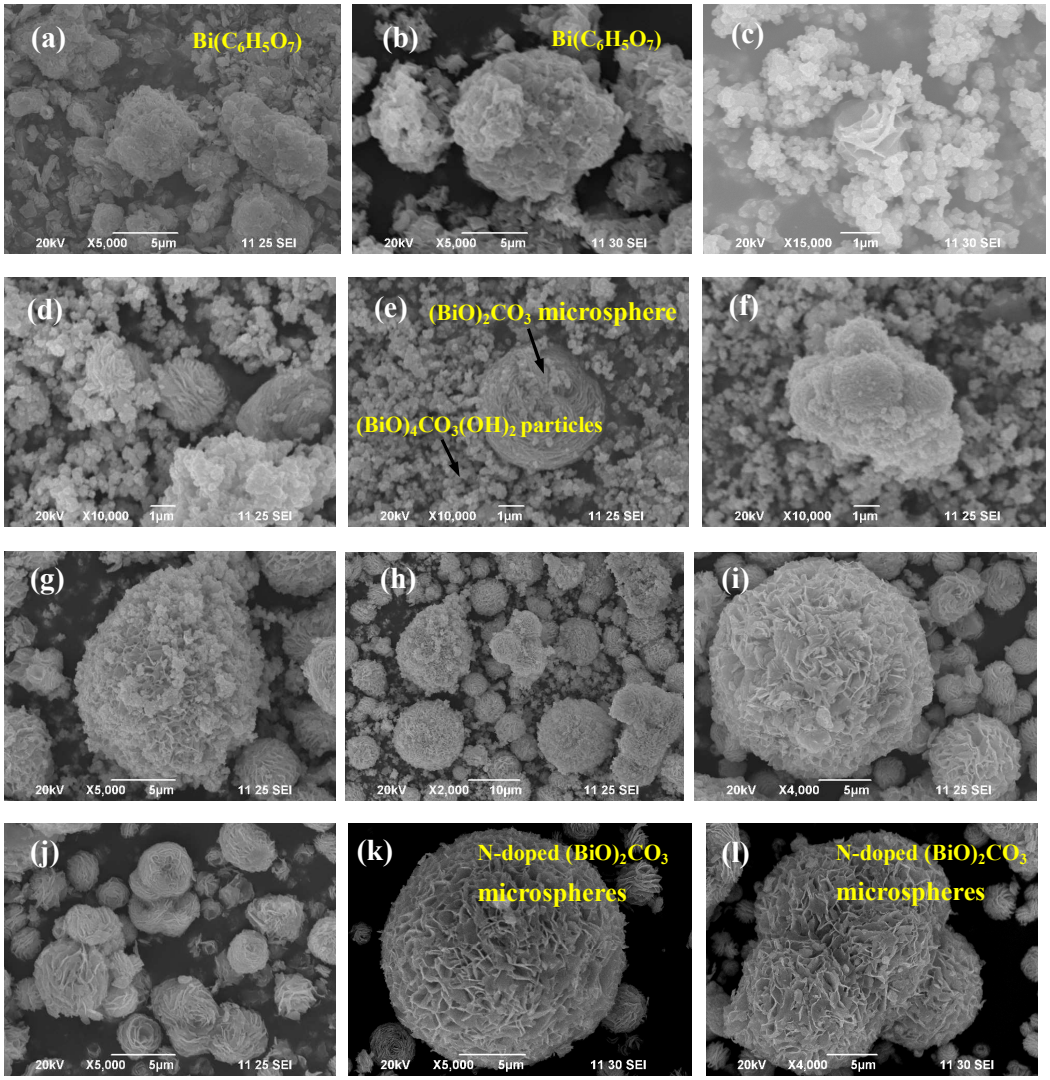

Fig. 3 SEM images of as-synthesized samples obtained at different hydrothermal time. (a) 0h, (b) 3h, (c) and (d) 6h , (e) and (f) 9 h, (g) and (h) 12 h, (i) and (j) 24h, (k) and (l) 48h.

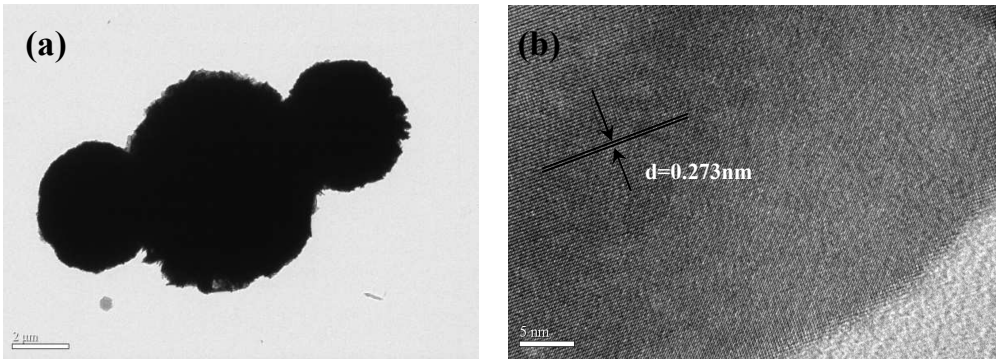

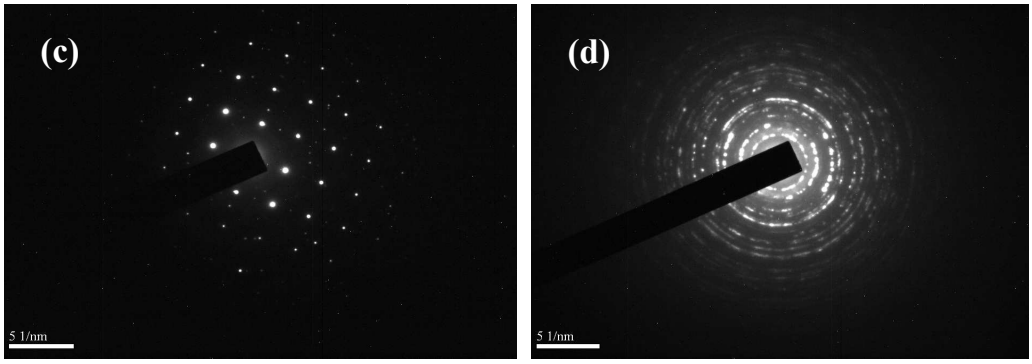

Fig. 4 TEM (a) and HRTEM (b) images of as-synthesized samples obtained at 48h, SAED of a single nanosheet (c) and individual N-doped $(BiO)_2CO_3$ microsphere (d).

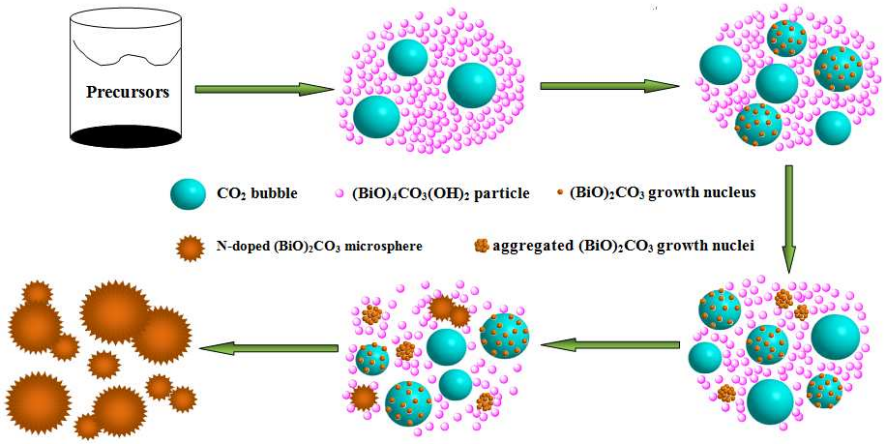

Scheme 1 The formation mechanism of self-organized N-doped $(BiO)_2CO_3$ microspheres

After 24h of hydrothermal treatment, large amount of particles dramatically decreased and microspheres self-assembled by nanosheets can be clearly observed, while few particles are still adhered to the surface of the microspheres (Fig. 3i and 3j). As all particles disappeared, fully-developed microspheres constructed by interconnected nanosheets are obtained when the reaction time is further extended to 48 h (Fig. 3k and 3l). The as-synthesized microspheres with diameters about 1.3 to 18.0μm are stacked together or dispersed, which confirms that the reaction system is not homogeneous. In addition, the interconnected nanosheets are densely assembled, and most of the nanosheets are arranged perpendicularly and pointed out from the center. More importantly, many pores are yielded associated with the aggregation of nanosheets, and these pores are highly desirable for photochemical applications because they can serve as transport paths for reactants and products.[38-39] Based on the SEM analysis, we can find that this process is akin to a gaseous template method. But quite differently, CO_2 bubbles as templates will take part in reaction in this study, namely, CO_2 bubbles can exist for a certain time because of the limited OH^-. With the release of OH^- (reaction (6)), CO_2 bubbles will vanish. Next, the $(BiO)_2CO_3$ growth nuclei on the surface of CO_2 bubbles aggregate together by the driving force, and further grow to be microspheres. Consequently, the eventually formative microspheres constructed by self-assembled nanosheets are not hollow but solid, which can be proved by the TEM result presented in Fig. 4a. The corresponding HRTEM image of a single nanosheet in a microsphere is shown in Fig 4b. The lattice fringe is about 0.273 nm, matching with the spacing of the (110) crystal plane of $(BiO)_2CO_3$. This result is also consistent with the XRD observation that the (110) diffraction peak is pronounced. The SAED pattern of one single nanosheet (Fig. 4c) displays an array of regular diffraction spots, indicating that the nanosheet is single crystalline. SAED pattern of a N-doped $(BiO)_2CO_3$ microsphere was also recorded in Fig. 4d. It is clear that the overall assembly of N-doped $(BiO)_2CO_3$ microsphere has a polycrystalline nature. Thus, the self-organized N-doped $(BiO)_2CO_3$ hierarchical microspheres are composed of single-crystalline nanosheets. The plausible formation mechanism of self-organized N-doped $(BiO)_2CO_3$ microspheres is proposed as systematically displayed in Scheme 1.

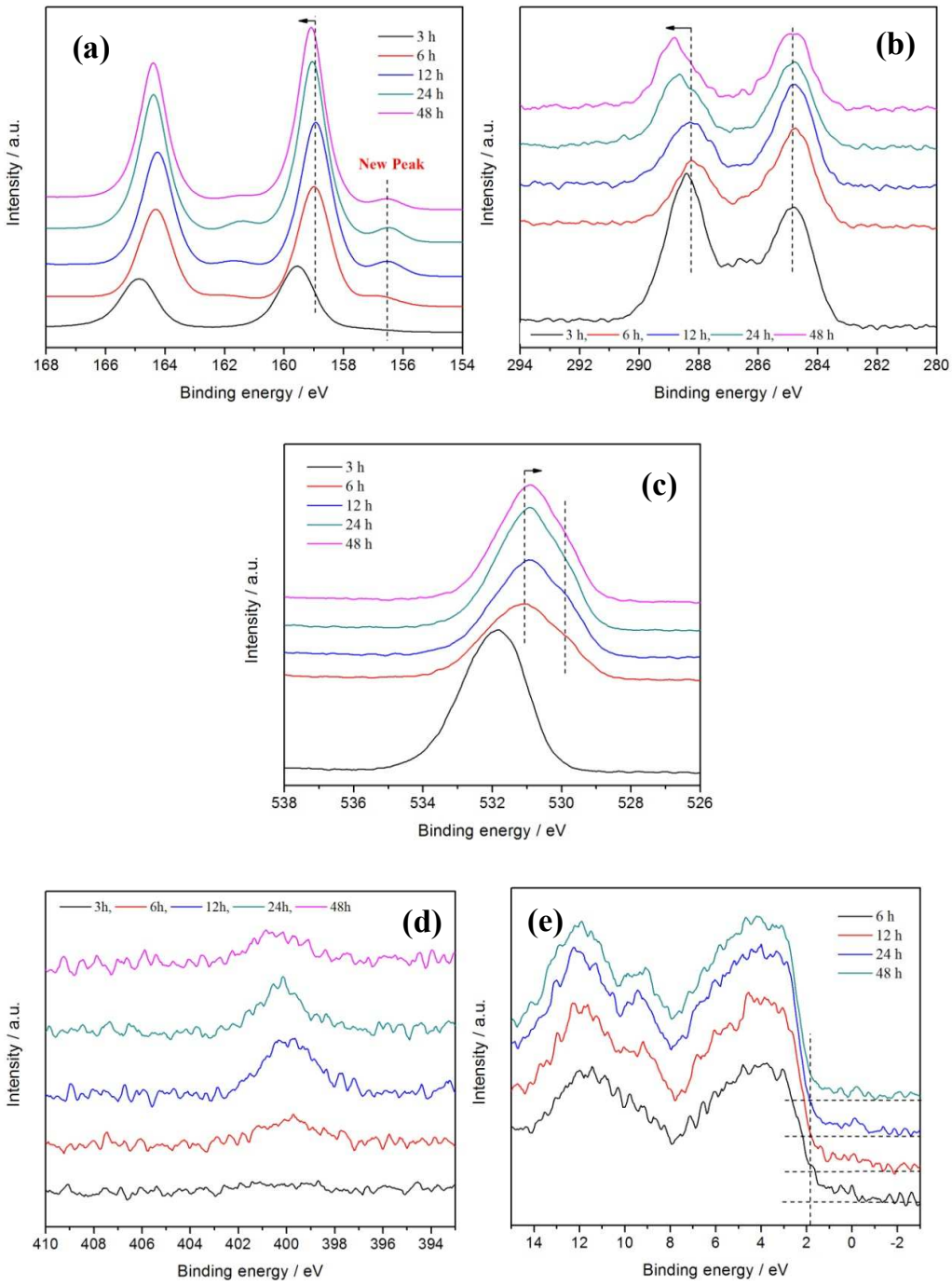

Fig. 5 XPS spectra of the samples for different reaction time from 3 to 48 h, (a) Bi4f, (b) C1s, (c) O1s, (d) N1s and (e) VB.

3.4 Chemical composition by XPS Analysis. To investigate the valance states and chemical environment of constituent elements on the surface of the self-organized N-doped $(BiO)_2CO_3$ microspheres, the as-prepared samples produced at different reaction time were examined thoroughly by XPS as depicted in Fig. 5. The Bi4f spectra for the samples are presented in Fig. 5a, two feature peaks of Bi^{3+} occur at ca. 159.5 eV and 164.9 eV in bismuth citrate. However, three peaks with binding energies of 156.6 eV, 159 eV and 164.8 eV appear in the sample hydrothermally treated for 6h. The peak located at 156.6 eV is indexed to the Bi4f peak of Bi element probably generating from the reduction of Bi^{3+} by urea, and the intensity of the peak increases with hydrothermal time. The other two peaks at 159 eV and 164.8 eV belong to $Bi4f_{7/2}$ and $Bi4f_{5/2}$ peaks of Bi^{3+} ion, respectively.[40] In

addition, positive shifts of the binding energy of the two peaks can be observed with the enhanced hydrothermal time, reflecting the phase transformation from $(BiO)_4CO_3(OH)_2$ to $(BiO)_2CO_3$. Because the electronegativity of OH^- is weak compared with CO_3^{2-}, the binding energy of Bi4f orbit in $(BiO)_2CO_3$ should be stronger than that of $(BiO)_4CO_3(OH)_2$. A broad binding energy for C1s ranging from 282 to 291eV can be observed as shown in Fig. 5b. All the samples show a peak at about 284.8 eV, which is attributed to the adventitious hydrocarbon from the XPS instrument. The peak at 288.4 eV can be observed in bismuth citrate, while the peak at 288.3 eV can be assigned to the carbonate ion in the sample achieved at 6h, and the chemical shift of the peak at 288.3 eV shifts to higher value with the increasing hydrothermal time.

As for the O1s spectra of the samples (Fig. 5c), only one peak located at 531.9 eV is indexed to the binding energy of O1s orbit in the bismuth citrate. Two peaks appear at binding energies of 529.8 and 531 eV for the sample from 6h of reaction, respectively. Among them, the former peak is a characteristic binding energy of O–Bi bond in $(BiO)_2CO_3$ and $(BiO)_4CO_3(OH)_2$, while the latter peak can be assigned to hydroxyl groups in $(BiO)_4CO_3(OH)_2$ accordingly.[28] The former peak slightly shifts to lower value with increased hydrothermal time. Nevertheless, the latter peak completely disappears for the sample prepared at 48h, which suggests the complete transformation of $(BiO)_4CO_3(OH)_2$ into $(BiO)_2CO_3$ phase. This result is consistent with the analysis revealed by XRD. Notably, Fig. 5d displays that N_{1s} peak centered at around 400.2 eV appears for the samples except $Bi(C_6H_5O_7)$, which indicates that nitrogen provided by urea is *in situ* doped into $(BiO)_2CO_3$ successfully and then modifies the band structure during hydrothermal treatment. In addition, the atomic concentration of N in the samples obtained at 6h, 12h, 24h and 48h is calculated to be 0.96%, 1.83%, 1.36% and 0.94%, respectively. It is surprising to find that the N concentration increases when hydrothermal reaction time is increased from 6 to 12h and then decreases with time from 12 to 48h, which is supposed to be associated with the reaction between $Bi(C_6H_5O_7)$ and the N element in $(BiO)_2CO_3$. The DOS of VB for the samples in Fig. 5e shows that additional electronic states appear above the VB edge for N-doped $(BiO)_2CO_3$ samples, implying the formation of a mid-gap above the VB because of the introduction of N element in $(BiO)_2CO_3$.[41] The hybridization of the N orbital with the VB orbital of $(BiO)_2CO_3$ results in the uplifting of the VB position, thus narrowing the band gap of $(BiO)_2CO_3$. Identical to the change tendency of N concentration, the VB position first shifts up and then down as hydrothermal time increases.

3.5 UV-vis DRS. The optical property of the self-organized N-doped $(BiO)_2CO_3$ samples prepared from different time were examined by the UV-vis DRS technique as shown in Fig. 6a. Initially at 3h time interval, the adsorption edge of the $Bi(C_6H_5O_7)$ sample is estimated at approximately 325 nm, which indicates that $Bi(C_6H_5O_7)$ only absorbs UV light. By increasing the reaction time to 6 h, the sample exhibits strong visible light absorption with a steep edge in the visible light region. Further extending the hydrothermal reaction time to 9h and 12h, the samples show an obvious red shift, which mainly caused by the doped nitrogen narrowing the band gap and then improving the ability to harvest visible light. However, the N content gradully decreases as the hydrothermal time increases from 12 to 48h as shown by XPS, which leads to the decrease in visible light absorption correspondingly. This can be explained by the reason that the visible light absorption is positively correlated with doped nitrogen concentration.[42] Moreover, the band gaps of as-synthesized samples estimated from the intercept of the tangents to the plots of $(Ahv)^{1/2}$ vs. photo energy (Fig. 6b) are 3.83, 3.08, 3.06, 2.31, 2.42 and 2.81eV, respectively, which are consistent with the change of visible light absorbtion. Anyhow, the enhanced ability to absorb visible-light of the sample (48h) makes it a promising photocatalyst for solar-driven application. Additionally, the spectra of samples obtained at 6h, 9h and 12h show two absorption edges, suggesting that the samples contain two semiconductors of $(BiO)_4CO_3(OH)_2$ and $(BiO)_2CO_3$, which agrees well with the XRD. The sample obtained at 24h also contains $(BiO)_4CO_3(OH)_2$ and $(BiO)_2CO_3$ according to the XRD analysis. Probably due to the amount of $(BiO)_4CO_3(OH)_2$ is small that it is beyond the detection of UV-vis DRS instrument, the sample obtained at 24h shows one absorption edge. Moreover, change of UV-vis DRS of the samples with reaction time is consistent with the VB observation in XPS (Fig. 5e).

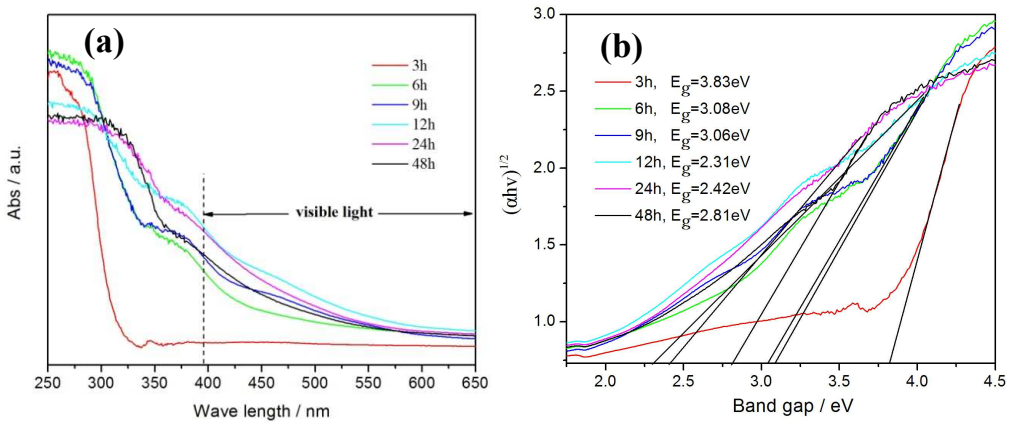

Fig. 6 UV-vis DRS (a) and the plot of $(\alpha h\nu)^{1/2}$ vs. photon energy (b) of the samples for different reaction time from 3 to 48 h.

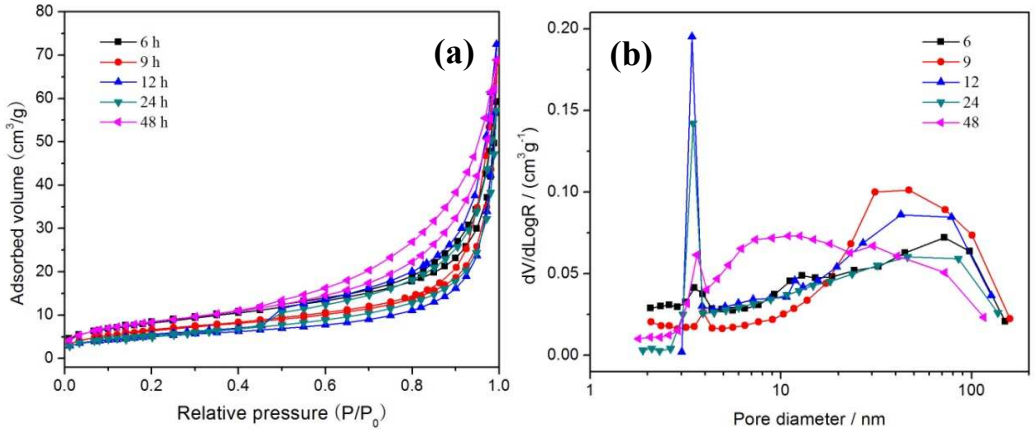

Fig. 7 N_2 adsorption and desorption isotherms (a) and pore-size distribution curves (b) of samples obtained at 6h, 9h, 12h, 24h and 48h.

3.6 Specific BET Surface Areas and Pore Structure. Fig. 7a shows the nitrogen adsorption-desorption isotherms of the samples obtained at different growth stages from 6 to 48h. These isotherms corresponding to all samples can be categorized as type IV with hysteresis loops observed in the range of 0.4–1.0 P/P_0, revealing the presence of mesopores.[43] Of the five samples, the shape of the hysteresis loops is of type H3, which is associated with the slit-like pores present in the samples.[43] All the samples show high absorption at high relative pressure (P/P_0) range (approaching 1.0), indicating the presence of macropores and mesopores.

The corresponding pore-size distributions (PSD) of the samples after hydrothermal treatment for different time are shown in Fig. 7b. Remarkably, the pores in all samples could be generally divided into two groups by their sizes according to the PSD curves: smaller mesopores of diameter less than 4 nm and larger pores with broad size distribution. The peak pore sizes of all samples are summarized in Table 1. For samples obtained at 6h, 9h and 12h, the smaller mesopores come from the stacked $(BiO)_2CO_3$ nanosheets, and the increase in peak intensity of smaller mesopores with hydrotherm time can result from the production of large amount of microsperes assembled by relatively dense nanosheets. The larger pores are formed between the $(BiO)_4CO_3(OH)_2$ particles. Because of the generation of smaller $(BiO)_4CO_3(OH)_2$ particles by dissolution-recrystallization process, the peak pore size of larger pores generated between particles decreases from 72nm to 43nm. For the samples achieved at 24h and 48h, the smaller mesopores may be created by the aggregation of the inner nanosheets which reflect the porosity within nanosheets,[34] while the larger pores can be attributed to the space between outer nanosheets of the microspheres. These pores might be extremely useful in photocatalysis since they provide efficient transport pathways to reactants and products.

Table 1. S_{BET}, peak pore size, and average pore diameter of the samples for different reaction time from 6 to 48 h

Samples	S_{BET} (m^2/g)	Peak pore size(nm)	Average pore diameter (nm)
6h	29.38	3.5/72	12.56
9h	22.93	3.9/47	18.77
12h	17.78	3.4/43	25.64
24h	19.01	3.4/46	17.67
48h	30.44	3.6/11	12.93

From Table1, we can find that the samples show a decrease in specific surface areas before 12h and then gradully display a slight increase with the increased hydrothermal time, and the trend of the change in S_{BET} is contrary to the average pore size. This result is consistent with the morphology change of the samples. As observed in SEM, the transformation from precursors to self-organized N-doped $(BiO)_2CO_3$ hierarchical microspheres undergoes a succession of steps including dissolution, reaction, crystallization, dissolution, recrystallization, dissolution, reaction and crystallization.

3.7 Photocatalytic activities under visible and UV light irradiation. The photocatalytic activities of the as-prepared samples were evaluated towards removal of NO under both visible light and UV irradiation, aiming at exploring the utilization percent of the solar light (Fig. 8). Fig. 8a shows the variation of NO concentration (C/C_0%) with irradiation time under the as-prepared samples obtained at different time when exposure to visible light irradiation. Here, C_0 and C are the concentration of NO at time zero and t, respectively. As a comparison, we test the photocatalytic activity of P25 under identical conditions. It is reported that NO could not be photolyzed without photocatalyst under light illumination.[40] As shown in Fig. 8a, P25 exhibits a removal rate of 10% mainly benefiting from its mix phases of anatase and rutile after 60 min irradiation. It also can be found that $Bi(C_6H_5O_7)$ has no visible light photocatalytic activity. Obviously, the photocatalytic activity of the as-prepared samples is enhanced with an increase in hydrothermal time, which are relevant to the phase transition from $(BiO)_4CO_3(OH)_2$ to $(BiO)_2CO_3$ and the formation of hierarchical structure. In addition, as the increase of hydrothermal time, the visible light absorption of the samples increases first and then gradully decreases as reveled by UV-vis analysis,

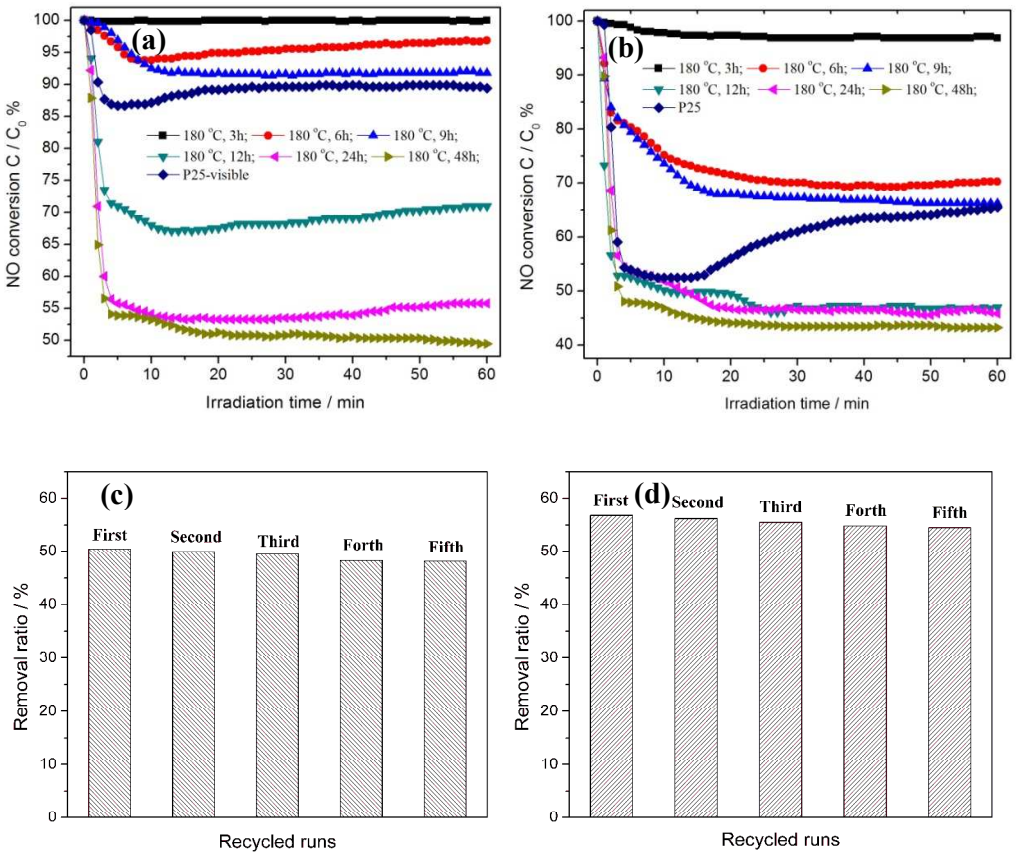

Fig. 8 Photocatalytic removal of NO in air in the presence of samples obtained from different reaction time from 3 to 48 h, together with P25 under visible light (a) and UV light (b) irradiation, and repeated visible light (c) and UV (d) light photocatalytic activities of self-organized N-doped $(BiO)_2CO_3$ hierarchical microspheres.

while the BJH result shows that the S_{BET} decreases first and then increases. It can be concluded that both S_{BET} and the N concentration can exert influence on the visible light activity. When the time is extended to 48h, the NO removal rate of the sample reaches up to 49.6% mainly due to the special hierarchical structure. Such special 3D hierarchical structure with meso- and/or macro- pores can serve as efficient transport paths for reactants and products in photocatalytic reactions.[38,39,44,45]

Fig. 8b shows the photocatalytic performances of different photocatalysts under UV irradiation. P25 is a well-known UV light photocatalyst, which shows relatively high activity with a removal rate of 35.1%. Only 4.2% of removal ratio towards NO can be observed when using $Bi(C_6H_5O_7)$ as photocatalyst, indicating its low photoresponse to UV light irradiation. Likewise, the UV light activity of the as-prepared samples increases as the hydrothermal reaction time increases. The removal rate of NO is up to 57% over the sample obtained at 48h upon the exposure of UV light irradiation for 60 min, which is much higher than that of P25 mainly due to the hierarchical structure as well, despite its BET surface area is smaller than that of P25 (51.2 m^2/g). Also, it implies that the surface area is not the main factor that affects the photocatalytic properties of the samples. In addition, The photocatalytic stability of photocatalysts during photocatalytic reactions is significant in view of its applications. To examine the photocatalytic stability of the N-doped $(BiO)_2CO_3$ sample (48h), the circulating runs in the photocatalytic removal of NO under visible and UV light irradiation were carried out. As shown in Fig. 8c and 8d, the N-doped $(BiO)_2CO_3$ sample still maintains relatively durable photocatalytic activity with no obvious deactivation after five repetitive cycles. This fact implies that the obtained N-doped $(BiO)_2CO_3$ sample have high stability. Note that the visible light activity of self-organized N-doped $(BiO)_2CO_3$ hierarchical architectures is comparable to the activity under UV irradiation. This fact indicates that the as-prepared samples are highly active under both visible and UV irradiation, which could make the as-prepared materials fully harness solar energy to remove environmental pollutants.

4. Conclusion

To sum up, we have demonstrated a one-pot additive-free fabrication of novel N-doped $(BiO)_2CO_3$ hierarchical microspheres self-assembled by nanosheets. On the basis of time-dependent observation of crystal structure and morphology, a formation mechanism for such hierarchical nanostructures was revealed, which involved an analogous gaseous template method. In this reaction system, CO_2 bubbles can act not only as gaseous template, but also as reactants participating in reaction, which resulted in the production of microspheres with solid centers. In addition, depending upon the distance between neighboring CO_2 bubbles, the resultant microspheres were either linked or dispersed. Also, the inhomogeneous release of CO_2 bubbles and CO_3^{2-} were contributed to different sizes of self-organized N-doped $(BiO)_2CO_3$ hierarchical microspheres. The as-prepared N-doped $(BiO)_2CO_3$ hierarchical microspheres exhibited outstanding and durable photocatalytic activities under both UV and visible light irradiation for NO removal, far exceeding that of commercial P25. The facile and convenient method, free of any additive, could be applied to synthesize other hierarchical materials with novel shape.

Acknowledgements

This research is financially supported by the National Natural Science Foundation of China (51108487), the Natural Science Foundation Project of CQ CSTC (cstc2013jcyjA20018), the Science and Technology Project from Chongqing Education Commission (KJ130725) and the Innovative Research Team Development Program in University of Chongqing (KJTD201314).

References

1 L. W. Zhang, T. G. Xu, X. Zhao and Y. F. Zhu, *Appl. Catal. B.*, 2010, **98**, 138.
2 M. P. Melancon, M. Zhou and C. Li, *Acc. Chem. Res.*, 2011, **44**, 947.
3 H. Y. Chen, D. B. Kuang and C. Y. Su, *J. Mater. Chem.*, 2012, **22**,15475.
4 M. D'Arienzo, L. Armelao, A. Cacciamani, C. M. Mari, S. Polizzi, R. Ruffo, R. Scotti, A. Testino, L. Wahba and F. Morazzoni, *Chem. Mater.*, 2010, **22**, 4083.
5 L. Xu, J. X. Xia, H. Xu, S. Yin, K. Wang, L. Y. Huang, L. G. Wang and H. M. Li, *Journal of Power Sources*, 2014, **245**, 866.
6 X. Y. Lai, J. E. Halpert and D. Wang, *Energy Environ. Sci.*, 2012, **5**, 5604.
7 J. H. Sun, J. S. Zhang, M. W. Zhang, M. Antonietti, X. Z. Fu and X. C. Wang, *Nat. Commun.*, 2012, **3**, 1139.
8 J. Wang, K. P. Loh, Y. Zhong, M. Lin, J. Ding and Y. Foo, *Chem. Mater.*, 2007, **19**, 2566.
9 I. D. Hosein and C. M. Liddell, *Langmuir*, 2007, **23**, 2892.

10 J. G. Yu, X. X. Yu, B. B. Huang, X. Y. Zhang and Y. Dai, *Cryst. Growth Des.*, 2009, **9**, 1474.
11 D. Yang, S. Chen, P. Huang, X. Wang, W. Jiang, O. Pandoli and D. Cui, *Green Chem.*, 2010, **12**, 2038.
12 C. Zhou, Y. F. Zhao, T. Bian, L. Shang, H. J. Yu, L. Z. Wu, C. H. Tung and T. R. Zhang, *Chem. Commun.*, 2013, **49**, 9872.
13 C. Zhou, G. Chen and Q. Wang, *J. Mol. Cata. A.*, 2011, **339**, 37.
14 J. X. Sun, G. Chen, J. Z. Wu, H. J. Dong and G. H. Xiong, *Appl. Catal. B.*, 2013, **132**, 304.
15 H. C. Zeng, *Current Nanoscience*, 2007, **3**,177.
16 B. Liu and H. C. Zeng, *Small*, 2005, **1**, 566.
17 H. J. Fan, U. Gösele and M. Zacharias, *Small*, 2007, **3**, 1660.
18 J. Zhang, F. Huang and Z. Lin, *Nanoscale*, 2010, **2**, 18.
19 J. X. Cui, W. S. Wang, L. Zhen, W. Z. Shao and Z. L. Chen, *CrystEngComm*, 2012, **14**, 7025.
20 K. X. Ren, K. Zhang, J. Liu, H. D. Luo, Y. B. Huang and X. B. Yu, *CrystEngComm*, 2012, **14**, 4384.
21 G. H. Jiang, X. H. Wang, Z. Wei, X. Li, X. G. Xi, R. B. Hu, B. L. Tang, R. J. Wang, S. Wang, T. Wang and W. X. Chen, *J. Mater. Chem. A.*, 2013, **1**, 2406.
22 Y. Zheng, F. Duan, M. Q. Chen and Y. Xie, *J. Mol. Catal. A: Chem.*, 2010, **317**, 34.
23 L. Chen, R. Huang, S. F. Yin, S. L. Luo and C. T. Au, *Chem. Eng. J.*, 2012, **193**, 123.
24 F. Dong, A. M. Zheng, Y. J. Sun, M. Fu, B. Q. Jiang, W. K. Ho, S. C. Lee and Z. B. Wu, *CrystEngComm*, 2012, **14**, 3534.
25 F. Dong, W. K. Ho, S. C. Lee, Z. B. Wu, M. Fu, S. C. Zou and Y. Huang, *J. Mater. Chem.*, 2011, **21**, 12428.
26 H. Bai, Z. Liu and D. D. Sun, *Chem. Asian J.*, 2012, **7**, 1772.
27 F. Zou, Z. Jiang, X. Qin, Y. Zhao, L. Jiang, J. Zhi, T. Xiao and P. P. Edwards, *Chem. Commun.*, 2012, **48**, 8514.
28 F. Dong, Y. J. Sun, M. Fu, W. K. Ho, S. C. Lee and Z. B. Wu, *Langmuir*, 2012, **28**, 766.
29 H. F. Cheng, B. B. Huang, K. S. Yang, Z. Y. Wang, X. Y. Qin, X. Y. Zhang and Y. Dai, *ChemPhysChem*, 2010, **11**, 2167.
30 P. Taylor, S. Sunder and V. J. Lopata, *Can. J. Chem.*, 1984, **62**, 2863.
31 J.D. Grice, *Can. Mineral.*, 2002, **40**, 693.
32 F. Dong, Y. J. Sun, W. K. Ho and Z. B. Wu, *Dalton Trans.*, 2012, **41**, 8270.
33 G. E. Tobon-Zapata, S. B. Etcheverry and E. J. Baran, *J. Mater. Sci. Lett.*,1997, **16**, 656.
34 F. Dong, S. C. Lee, Z. B. Wu, Y. Huang, M. Fu, W. K. Ho, S. C. Zou and B. Wang, *J. Hazard. Mater.*, 2011, **195**, 346.
35 X. Y. Chen, Z. H. Wang, X. Wang, R. Zhang, X. Y. Liu, W. J. Lin and Y. T. Qian, *J. Crys. Growth*, 2004, **263**, 570.
36 H. Z. Wang, J. B Liang, H. Fan, B. J. Xi, M. F. Zhang, S. L. Xiong, Y. C. Zhu and Y. T. Qian, *J. Solid State Chem.*, 2008, **181**, 122.
37 X. Y. Che, Z. J. Zhang, X. X. Li and C. W. Shi, *Chem. Phys. Lett.*, 2006, **422**, 294.
38 F. Dong, H. T. Liu, W. K. Ho, M. Fu and Z. B. Wu, *Chem. Eng. J.*, 2013, **214**, 198.
39 F. Dong, T. Xiong, Z. W. Zhao, Y. J. Sun and M. Fu, *CrystEngComm*, 2013, **15**, 10522.
40 Z. H. Ai, W. K. Ho, S. C. Lee and L. Z. Zhang, *Environ. Sci. Technol.*, 2009, **43**, 4143.
41 X. B. Chen and C. Burda, *J. Am. Chem. Soc.*, 2008, **130**, 5018.
42 F. Dong, S. Guo, H. Q. Wang, X. F. Li and Z. B. Wu, *J. Phys. Chem. C.*, 2011, **115**, 13285.
43 K. S. W. Sing, D. H. Everett, R. A. W. Haul, L. Moscou, R. A. Pierotti, J. Rouquerol and T. Siemieniewska, *Pure Appl. Chem.*, 1985, **57**, 603.
44 J. G. Yu, Y. R. Su and B. Cheng, *Adv. Funct. Mater.*, 2007, **17**, 1984.
45 X. X. Yu, J. G. Yu, B. Chen and M. Jaroniec, *J. Phys. Chem. C.*, 2009, **113**, 1752.

Table of contents entry.

A new growth mechanism was proposed for the self-organized N-doped $(BiO)_2CO_3$ hierarchical nanosheets microspheres with efficient and durable photocatalytic activity.

TOC Graphic